Dissimilar Cladding of Ni–Cr–Mo Superalloy over 316L Austenitic Stainless Steel: Morphologies and Mechanical Properties

A. Evangeline[1] · P. Sathiya[1]

Abstract

The solid solution strengthened Inconel 625, a Ni-based alloy is known for its excellent strength and good corrosion resistance at extreme environments used in thermal plants, boiler tubes, petrochemical industry and power plant. The presence of Cr content (~20 wt%) along with Mo-rich, Nb and Fe makes Ni–Cr–Mo–Nb austenitic alloy called as Inconel 625 to achieve excellent corrosion resistance property. Using cold metal arc transfer (CMT) cladding, the metallurgical, mechanical and corrosion properties of Inconel 625 on 316L is evaluated. The process parameters selected includes welding current, torch angle and travel speed with a constant voltage. From the results of microstructural and EDS inferences, the formation of cellular dendritic structure with secondary phases like Laves phase, complex nitrides along with the interdendritic segregation of Mo and Nb as well as microsegregation of Cr, Ni and Fe. In case of Ni–Cr–Mo alloy, Ni and Cr contribute to resistance to corrosion in NaCl environments. The formation of Cr_2O_3 and the passivation action of the clad zone is due to the presence of Cr. The solid solution effect in Ni–Cr matrix is contributed by the presence of Nb and Mo. Apart from that the strengthening action happens due to the precipitation of Ni_3 (Al, Ti, Nb) commonly known as γ′, γ″ and MC carbides confirmed through XRD. Uni-axial tensile tests and Vickers-micro hardness indentation tests were performed on Inconel 625 cladded over 316L. Based on the fractographic results fatigue striations, tear rigdes with river markings, dimples with fibrous structure and cleavages are observed. Unlike other studies, unique type of cuboidal precipitates are seen, which is due to the presence of Ti, which form carbonitrides containing Ti, which are further characterised as NbC. The potentiodynamic polarisation tests is performed on 3.5% NaCl solution. The results suggest that Ni–Cr–Mo alloy protects the substrate from corrosion.

Keywords Cold metal arc transfer cladding · Inconel 625 · 316L · Potentiodynamic polarisation tests

1 Introduction

Application of Ni-based Inconel 625 includes power plants, boiler tubes, chemical plants and thermal station due to their excellent performance at high temperature [1, 2]. The outstanding commercial grade Ni–Cr–Mo alloy also known as Inconel 625, which contains secondary intermetallic phases like Laves phases along with Nb and Fe, is used mainly because of its notable strength, good fabricability and outstanding corrosion resistance [3]. Owing to its high cost and also to protect cheaper base material from corrosion, Inconel 625 is used. To perform the Ni-base clad layers with negligible Fe content, a revolutionary GMAW technique called Cold Metal arc Transfer (CMT) was used. Invented by Fronius, CMT [4] contains droplet deposition by wire detachment through wire-motions embedded in the digital process-control. The advantage of Cold Metal arc Transfer (CMT) over Cold Arc (CA) is that CMT puts a unique wire feed system through digital control for achieving controlled droplet deposition with low amount of heat. CMT is advantageous than CA in case of cladding of dissimilar alloys pertaining to its low heat input which confines the appearance of brittle intermetallic compound [5].

The droplet deposition assisted by short circuiting is possible through the retraction motion of the wire was coined by Kah et al. [6]. The findings of Schierl [7] revealed that, CMT offers less spatter. The fundamentals and principles of short circuiting and droplet detachment motion of CMT cladding are observed by Pickin and Young [8]. Findings reported by Zhang et al. [9] reveals that the application of CMT in dissimilar cladding of Ni-based alloys prevents appearance

✉ P. Sathiya
  psathiya@nitt.edu

[1] Department of Production Engineering, National Institute of Technology, Tiruchirappalli, Tamil Nadu 620015, India

of intermetallic compounds, owing to the advantage of low heat input.

The Ni-based superalloy is known as complicated type of superalloy, because of its many phases [10]. The Ni-based superalloy contains carbides, austenitic matrix γ and tenacious sediments of γ′ [11–14]. The two types of Ni-based superalloy are solid solution type and precipitation hardening type. The austenitic matrix phase containing FCC network along with the secondary phases containing FCC carbides (MC and $M_{23}C_6$), γ″ phase (Ni_3Nbi), are observed in microstructural characterisation of Inconel 625.

The loss prone by the high temperature Inconel 625 superalloy at elevated temperature includes abrasion, corrosion, and oxidation [15–18]. Hence, samples should be cladded in order to protect the surfaces from damage.

Abioye et al. [19] in their work on Inconel 625 cladding over AISI 304, from the microstructural analysis reveal the presence of formation of dendrite background phase along with the precipitates of carbides in γ background and appearance of eutectic phase (Laves phase). At the clad region and also on the interface region towards the clad, formation of columnar and cellular dendrites are confirmed by Dinda et al. [20].

The deposition of Inconel 625 on carbon steel using CMT exhibits segregation of Ni, Mo, Nb and Cr along the dendrite core. Rozmus et al. examined the cladding of Ni–Cr–Mo alloy using GMAW, GTAW and CMT and identified that the metallurgical and mechanical properties of cladding relay on the process applied and the as received chemical composition of the base material. Ola et al. studied about CMT cladding of Inconel 718 filler over the same substrate and found out that defect free clads with less than 10% dilution is possible.

Xu et al. [21] evaluated the cladding microstructural inferences of Inconel 625 over 316L stainless steel substrate. From the findings the columnar and coaxial dendrites were seen in the cladded and interface zone towards the clad cellular structure is observed along with γ phase. Verdi et al. [22] worked on Inconel 625 cladded over Gr_{22} ferritic steel (ASTM A387) base material and observed similar results to that of previous studies. DuPont [23] identified that using TIG cladding of Inconel 625, γ + Laves phase are produced during crystallization and derived the following:

$$L \rightarrow \gamma \rightarrow L + \gamma \rightarrow L + \gamma + \text{Laves} \rightarrow \gamma + \text{Laves.} \quad (1)$$
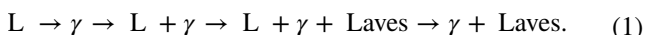
The Nb and Mo get separated from the phases formed at high remperatures. Limited studies are performed on the metallographical aspects of CMT cladding using Ni-based superalloy [23].

Lots of experimental work were done to identify the solidification action of Nb present in the Ni-based superalloys. DuPont and Robino [24] findings revealed that solidification of Inconel follows three stages, which are: (1) solidification occurs at the primary stage $L \rightarrow \gamma$, (2) a reaction occurs at eutectic stage $L \rightarrow (\gamma + NbC)$, at a wide range of temperature, (3) a reaction at the eutectic terminal stage $L \rightarrow (\gamma + \text{Laves})$ occurs at lower final temperature. Recent research exemplifies that precipitates present in Nb, C, N and Ti during the dissimilar welding of Inconel 625, can change the solidification behaviour of the alloys [25–28]. Due to the combined effect of microchemical and microstructural inferences during the solidification of Ni-based alloys, there exist a new relationship between the metallurgical and mechanical properties of Ni-based alloys.

From the past literatures it has been inferred that cladding of dissimilar materials by proper implications of cladding conditions, there occurs changes in the chemical composition due to improvement of Fe and C present in Ni–Cr–Mo alloy results in changes in partially melted zone [29, 30]. Similar studies have found out that the precipitates of Ni, Cr, Nb and Ti can change the solidification behaviour of the alloy.

Many research have been conducted on metallurgical and phasic formation of variety of similar cladding with Inconel–Inconel [31]. The cladding of Inconel 625 using CMT technique seems to be revolutionary and potentially tensile stresses developed during the weld cooling cycle, producing microfissuring high temperature applications. Very few information have been given about the dissimilar bonding between Inconel 625 and 316L in terms of formation of secondary precipitates and segregation of Mo. Here a unique cubic precipitates rich in Ti, having a complex structure containing titanium nitrite encompassed by NbTiC is observed through SEM.

2 Material and Sample Preparation

The required samples of dimension 200 mm × 100 mm x 10 mm thickness are cladded with Inconel 625 over 316L. Table 1 shows the as received chemical composition 316L stainless steel. Inconel 625 filler wire of diameter 1.2 mm is used and the chemical composition is clearly listed in Table 1.

The clad, interface and the substrate region of the sample was thoroughly polished using SiC papers made of grit size 220, 400, 600, 800, 1000, 1200 and also cleaning them with acetone prevents the sample from oxidation and other contaminants.

2.1 Cold Metal Arc Transfer (CMT) Cladding Process

Fronius CMT 7000 VR machine is used in cladding of Inconel 625 over 316L substrate as shown in Fig. 1. The greater contact angles are possible with pulsed-CMT mode when compared with the conventional type of CMT mode.

Table 1 As received chemical composition of 316L and Inconel 625

Base metal—AISI 316L wt%

C	Mn	Si	Cr	Ni	Mo	P	S	N	Fe
0.02%	2.00%	0.75%	16.00%–18.00%	10.00%–14.00%	2.00%–3.00%	0.05%	0.03%	0.10%	Bal.

Filler wire—Inconel 625 wt%

Cr	Ni	Mo	Co	Nb + Ta	C
20%–23%	58–Bal%	8%–10%	0%–1%	3.1%–4.1%	0%–0.1%
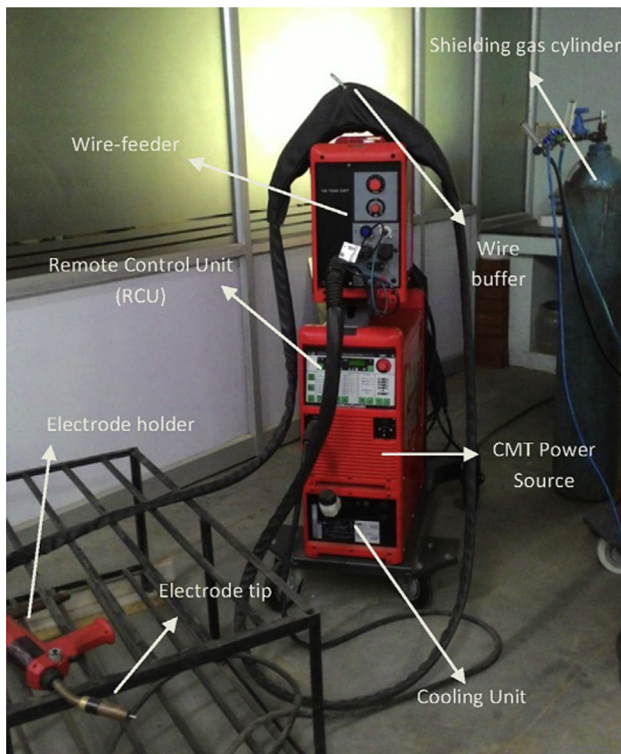
Fig. 1 Fronius CMT 7000 VR machine set up

The variations in speed can be controlled using 6-axis Yaskawa Motoman robot. The robotic arm controls the travel speed and path while other welding parameters torch angle, voltage and current can be controlled in remote control unit (RCU) inbuilt in the CMT Fronius system.

Argon as a shielding gas with the flow rate of 15–20 L/min is used. The nozzle diameter is around 3.2 mm. 70 bar of cylinder pressure is maintained. The quality of the clad bead lies on the selected process parameters. The welding current (140, 160 and 180 Amps) voltage (17 volts), torch angle (60°, 70° and 80°), travel speed (125, 175 and 150 mm/min) are taken as the cladding process parameters, respectively. The welding current has a direct influence on depth of penetration and extends up to the fusion zone on the base metal. The shape and bead appearance are controlled and directed

Table 2 Experimental parameters

Exp. no.	Welding current (Amps)	Voltage (v)	Torch angle (deg)	Welding speed (mm/min)
Symbol	(I)	(V)	(TA)	(S)
C1	140	21	80	175
C2	160	21	60	150
C3	180	21	70	125

by the welding arc voltage. Similarly, travel speed has a direct influence on clad bead and depth of penetration for a given welding current and corresponding voltage.

Based on the trial and error runs, for welding current of 140 A, 160 A and 180 A corresponding samples C1, C2 and C3 were selected respectively. The parameters are shown in Table 2.

2.2 Microstructural Analysis

Before cladding of Inconel 625, the substrate 316L surface was ground with 120 grit SiC paper and then cleansed thoroughly with acetone. Again after cladding, the bead and the substrate were cleansed with the help of wire brush before each subsequent metal deposition.

Inconel 625 cladded on 316L plates of dimension $500 \times 100 \times 10$ mm were drawn into required length, further drawn into strips of dimension with the help of MW250 a high-precision micro wire cutting EDM into dimensions of $500 \times 10 \times 10$ mm. Further the samples were sliced down with the help of Master SSA abrasive cutting machine into dimensions of $20 \times 10 \times 10$ mm thickness.

The cladded samples C1, C2 and C3 were swabbed with ethanol prior to cladding inorder to get rid of impurities, such as grease and oil, which are usually present soon after the EDM cutting process. Transverse section of the clad beads follow standard metallographic procedure while polishing the samples. The polishing by SiC emery papers of grades 220, 400, 600, 800, 1000 and 1200 were done for microstructural characterization. The electrolytic etching applied for Inconel 625 includes 10% of ammonium

persulphate solution at 3.5 V for 5 s and etchants applied for base 316L includes concentrated aqua regia (3:1) 3HCl:HNO$_3$ for a minute.

To obtain microstructural characterization of the transverse cross sections of the Inconel 625, cladded sample was investigated with the help of LYNX Stereozoom Microscope with 5 MP C MOS Camera along with the Image Acquisition Software. The elemental phasic characterization of the sample comprising substrate, interface and clad region were investigated using scanning electron microscopy (SEM) (Hitachi S-3000 H) connected with energy dispersive spectrometer (EDS). X-ray diffraction (XRD) was acquired to determine phasic formation.

2.3 Microhardness Measurement

The measurement of microhardness was done with the help of Vickers microhardness indentation tester with ASTM E384 (Make: Wilson Hardness 402 MVD) with a loading force of 500 gf and dwell time of 10 s. Microhardness of the samples were evaluated from the center of the clad region towards the topmost surface of the base metal to its bottom with a spacing of 2 mm between successive points.

The readings are measured initially from the topmost clad region, then gradually moving towards the interface and base region, perpendicular to the direction of cladding.

2.4 Tensile Testing

Using Instron universal testing machine (UTM), the uniaxial tensile testing was performed on the samples C1, C2 and C3 as per ASTM: E8/8 M standard.

The tests performed on the base, interface and clad region, each distinctively from three different heat input taken from (Table 2) as shown in Fig. 2. A 50 kN UTM is used along with 1 mm/min cross head speed. The samples C1, C2 and C3 region of the clad, interface and base region are sliced parallel to the direction of cladding. The

sliced samples consists of 1 mm thickness respectively. From the past literatures, the samples with 10 mm gauge length are similar to that of micro tensile samples taken for analysis [32].

2.5 Potentiodynamic Polarization Technique for Corrosion Resistance

The corrosion behavior of Inconel 625 clad samples of dimensions 20x10x10 mm, are investigated using potentiodynamic polarization test at 24 °C in 3.5% NaCl solution, and it was performed as per ASTM G61-86 standard using IVIUM electrochemical workstation. The workstation contains one reference electrode composed of saturated calomel electrode (SCE), one counter electrode composed of graphite and sample acts as working electrode.

Initial delay of 10 s is given in order to generate an open circuit potential (OCP). Keeping scan rate at 0.8 mv/s, corresponding Tafel plot was calculated between −1 v/SCE to +1 v/SCE for samples C1, C2 and C3. The necessary parameters are calculated once the IVIUM soft electrochemistry software gets installed. The rate at which the samples gets corroded and corrosion current density are formulated by the following equation [32]:

$$\text{Corrosion rate} = 0.13 * I_{corr} * E.W./A * d \tag{2}$$

where I_{corr}, corrosion current density; E.W, equivalent weight of the sample used in (g/eq); A, area in cm^2; d, density (in g/cm^3).

The equivalent weight of 316L substrate is found to be of 25.50 g/eq and density of 8 g/cm^3. Similarly, equivalent weight of Inconel 625 filler wire found to be of 25.573 g/eq and density of 8.44 g/cm^3. Chemical composition of 316L base and Inconel 625 filler wire are tested initially and then obtained microhardness values are 218 HV$_{0.5}$ and 231 HV$_{0.5}$ and calculated corrosion density of round 8.73E−06 A/cm^2. Further SEM analysis followed by EDAX is taken for the respective corroded surfaces [33].
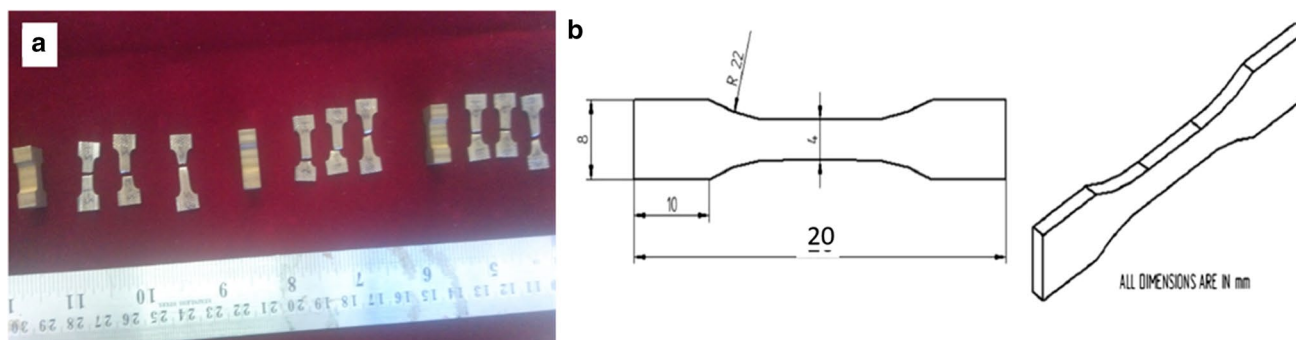

Fig. 2 Geometric profile **a** sliced tensile samples from base, interface and clad portion. **b** Required details about sample dimension

3 Results and Discussion

3.1 Macrostructure of the Cladding

The clad bead appearance of Inconel 625 on substrate 316L is shown in Fig. 3.

C1, C2 and C3 in Fig. 4a–c shows the measured depth of penetration (DOP) region and dilution of the clad bead.

The depth of penetration calculated from the stereozoom macroscope at a magnification of 20× has a linear relation with the heat input produced in the samples. As welding current increases, heat input also increases, but decreases with travel speed [33].

Heat input H is drawn from the following relation [34],

$$H = \frac{(0.06 \times V \times I)}{S} \tag{3}$$

where V, voltage in volts; I, welding current in ampere; S, welding speed in mm/min.

From Eq. (3), the required heat input for the sample C1, C2 and C3 are summarised in Table 3. From the findings of Kumar et al. changing of welding current and travel speed, brings a change in the depth of penetration and hence increases heat input along with the depth of penetration [35]. From Fig. 4 a–c, it is observed that in sample C2 (Fig. 4b) because of its inverse relationship with the travel speed, attains lower heat input. The calculated heat input in kJ/mm for C1, C2 and C3 samples (0.856, 0.669 and 0.918) respectively. The selected parameters for cladding for the respective sample C2 is found to be satisfied with the depth of penetration (520 µm) and with the lowest heat input.

The clad bead portrays highly smooth geometric configuration and without any undercut or cracks.

The transverse appearance of the bead shows the connection between bead geometry and process parameters. The geometry changes in accordance with welding current.
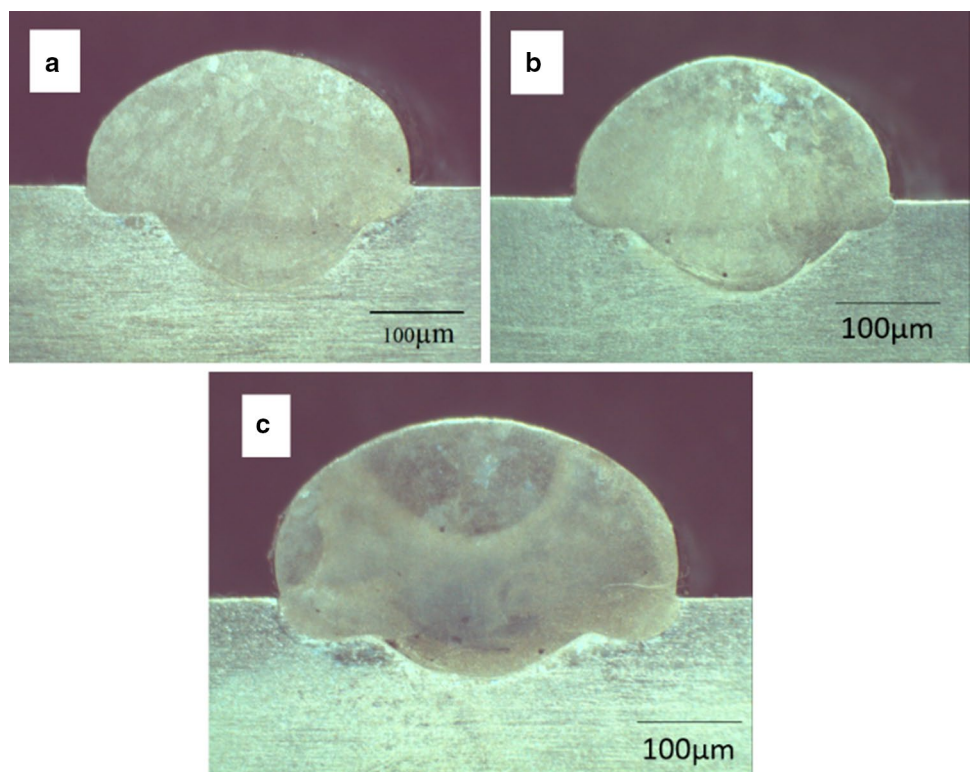

Fig. 3 Typical appearance of the clad bead

Table 3 Heat input for the samples C1, C2 and C3

Sample	C1	C2	C3
Heat Input (kJ/mm)	0.856	0.699	0.918

Fig. 4 Stereo macrographs of sample (**a**) C1, (**b**) C2 and (**c**) C3, respectively

Depending on the amount of heat input, the welding current increases (140 A, 160 A, 180 A) with an increase in depth of penetration and wider beads are achieved. Increase in percentage of dilution increases the welding current [27]. Increase of heat input, decreases the surface tension, as rise of liquid metal temperature results in wettability action.

Increase of heat input, increases the welding current but decreases the welding speed [33].

The calculated heat input for the sample shown in Eq. (3) are projected in Table 3. The investigation made by Kumar et al. by varying both welding current and travel speed, increase in depth of penetration is achieved along with the heat input [35].

From Eq. (3), the calculated Heat input in kJ/mm are tabulated in Table 3.

The observed heat input (0.856–0.699 kJ/mm) decreases with the increase of welding speed (125–175 mm/min). The microstructural investigation of the cladded samples based on the selected parameters ends up in good clad qualities with no porosity nor spatter along with lesser dilution (9.3%) found for C3 and high aspect ratio (2.6). Since CMT is a constant current process, the efficiency of the deposition remains constant, while bead width and depth increases with reduction in reinforcement height. The uniqueness of CMT is that as heat input increases, metal deposition also gets increased. Thus a portion of heat input gets consumed in the melting process, so spreading ability of the droplet on the base plate increases.

The clad beads were observed to be defect free with no pores as shown in Fig. 4a–c. Based on clad bead geometry analysis, sample C3, (I = 180 Amps, V = 17 volts, TA = 80° and S = 175 mm/min), results in minimum dilution and more bead width. The higher heat input of C3 sample is the reason behind minimal dilution. Heat transfer occurs at the interface containing Inconel 625 with 316L due to the effect of heat conduction from the melt pool to the base metal 316L. Figure 4a–c shows the dilution and bead geometry of the cladded portion and Table 4 presents the comparison of process parameters and measured bead profiles.

Using metallographic method, the dilution (D) are measured from the geometric cross sectional areas of the clad region i.e.) filler metal and base region i.e.) substrate. The ratio of area of substrate (A_s) to the total cross sectional area from the filler metal region and substrate ($A_s + A_{fm}$) gives the dilution value ($D = \frac{A_s}{A_s + A_{fm}}$).

The grain size measurement are carried out using Image analysis (ASTM E112) using Dexel Metallography software on the microstructural images taken at 200X zoom magnification in the transverse direction.

3.1.1 Direct Effect of Process Parameters on the Geometry of Clad Bead

The geometry of the clad beads were analysed. The dilution (%), depth of penetration (mm) and heat input (kJ/mm) were calculated see Table 4. The geometry of the clad beads were characterised by using optical microscopy (OM) for each sample (C1, C2 and C3) for three different trails of welding current (I) and travel speed (S). Few findings are drawn from the experimental trials. Increase of welding current increases the bead width, reason may be attributed to high magnitude of current producing greater force on the molten metal droplet enabling the spattering action which keeps the welding current constant as welding speed increases. Thus less amount of metal gets deposited over the substrate and ultimately lesser driving force is utilised for the molten weld pool to create bonding strength on the base metal. The heat input has an adverse effect on the depth of penetration since it is proportional to the current (owing to the combination of increased centrifugal and coulomb's forces). As current increases, reinforcement height decreases, reason due to the depth of penetration and the force created on the molten metal pool, at an increased welding speed.

3.2 Microstructural Analysis

The microscopic analysis obtained from the optical microscopy revealed that cladding of Inconel 625 over 316L produces no porosity, zero incomplete fusion and spatter free or no other flaws with minimal cracking and contains excellent metallurgical adhesion to the steel substrate as shown in Fig. 5a–e.

The microstructural image of cladded portion containing Inconel 625 clad layers comprises of cellular-dendritic

Table 4 Comparison of process parameters and measured bead profiles

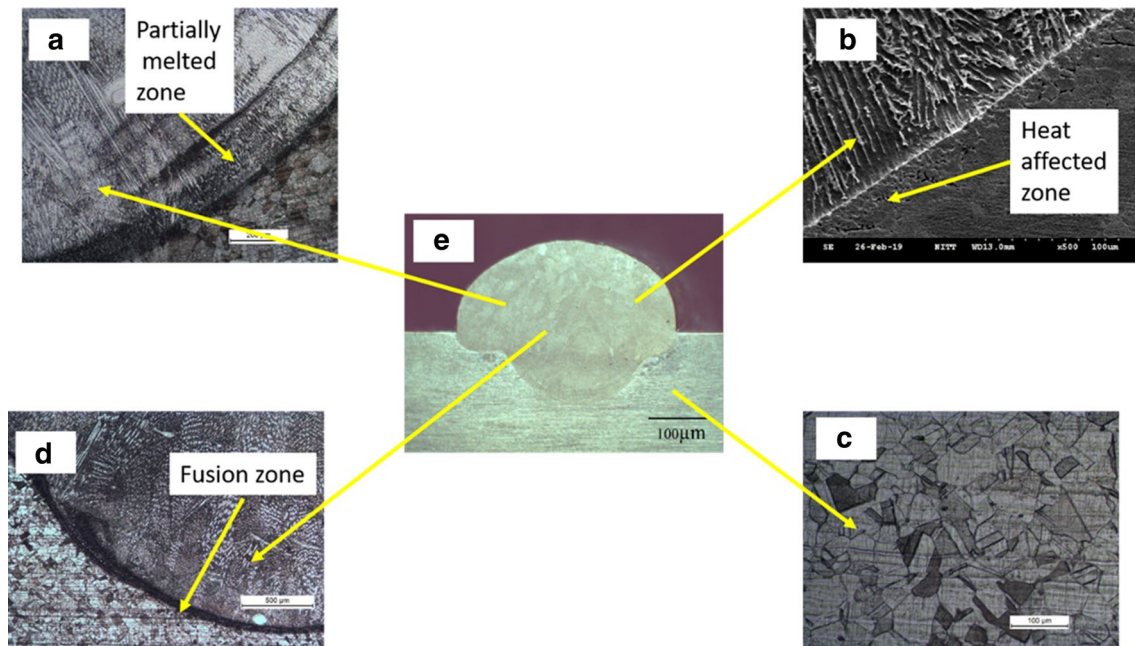| S. no.	Current I (Amps)	Voltage (v)	Torch angle (deg)	Welding speed, S (mm/min)	Depth of penetration, (mm)	Heat input (kJ/mm)	Dilution D (%)	Average grain size (μm)
C1	140	17	60	125	7.613	0.856	35.71	15.8
C2	160	17	70	175	2.443	0.699	28.5	19.3
C3	180	17	80	150	2.342	0.918	9.3	17.8

Fig. 5 Typical microstructural image of Inconel 625 on 316L. (**a**) partially melted zone (**b**) HAZ regio (**c**) substrate region (**d**) fusion boundary zone

structure. The growth of the dendritic arm lies parallel to the heat flow direction as shown in Fig. 5b.

The Inconel 625 cladding by cold metal arc transfer process allows rapid solidification process to take place which starts with formation of γ phase. For Inconel alloys, with absence of Nb composition, L/γ transformation is identified in non eutectic reaction [21, 22]. The Nb or B composition in Inconel 625 [23, 24] forms precipitates close to the interface region shown in Fig. 6. The solubility nature of Nb and Mo in Nickel is minimised by the presence of other alloying elements. Dendrites with γ phase appears as there is a drop in the level of liquid solidification. Remaining part of the liquid contains Nb and Mo. The segregation of dendrites rich in Nb and Mo at the fusion boundary regions, may be reason behind the formation of interdendritic region [12].

Scanning electron microscopy analyses the metallurgical characteristics of the cladding. The presence of γ phase and secondary phases are shown in Fig. 7. Elemental distribution spectroscopy results for Inconel 625 cladded region along with elemental mapping are revealed in Fig. 9c. The results of SEM–EDS reveals that due to strong segregation, the Ni and Cr move to the dendritic regions and diffusion action takes Mo and Nb to the interdendritic region.

From Fig. 7, the segregation action of Nb, results in Laves or NbC like secondary phase formation. Du Pont et al. [24] findings reveal that the succession of formation of NbC and Laves phase in Ni–Cr–Mo superalloy (~ 3.5 wt% of Nb) brings the following:
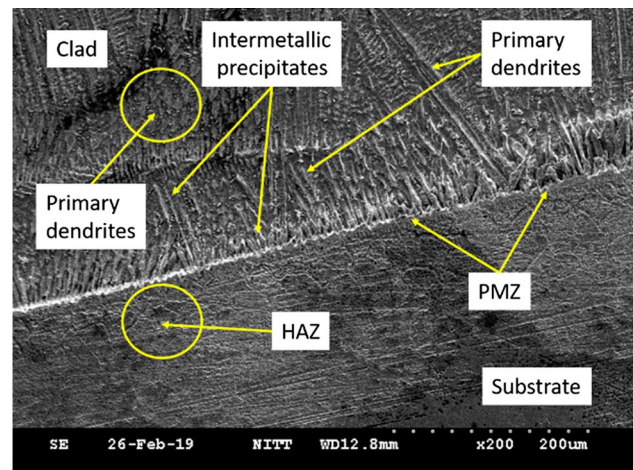
$$L \rightarrow L + \gamma \rightarrow L + \gamma + NbC \rightarrow \gamma + NbC + Laves.$$
(4)

Fig. 6 Fusion zone containing Inconel 625 cladded over 316L is shown at higher magnification

From the SEM inferences, the MX precipitates and γ matrix are observed in the clad portion of Inconel 625.

Formation of primary Ni-based γ matrix is visible on the clad region and secondary solidification micro constituent elements are seen along the interdendritic region. From Fig. 8 C1 sample with the lower current of 140A, shows intergranular microfissuring in partially melted zone (PMZ), and absence of liquation is observed in the samples C2 and C3.
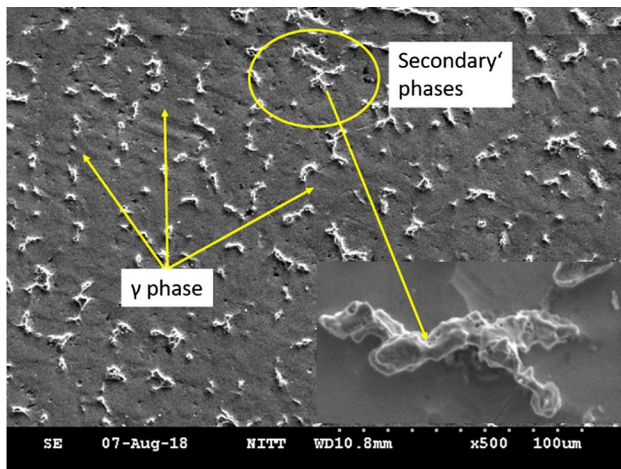
Fig. 7 SEM micrograph taken along the Inconel 625 Clad region showing Laves phase as well as secondary phase formation
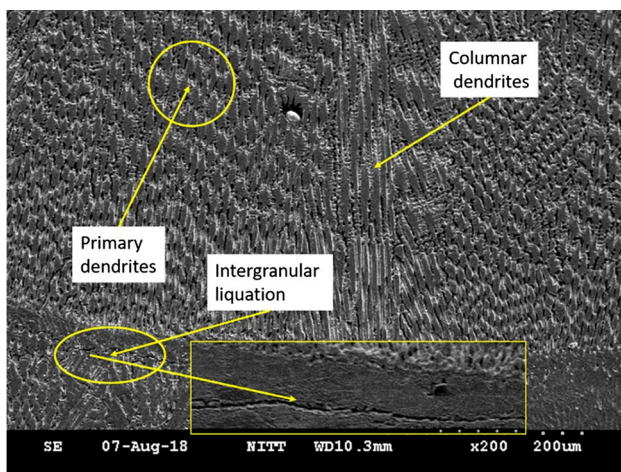

Fig. 8 A minimal intergranular liquation zone in HAZ shown in sample C1

The intergranular liquation initiates microfissuring in Ni–Cr–Mo alloys. From the previous studies microfissuring are not observed in CMT. Present work stays as an exception from other studies. The reason for the occurrence of microfissuring is due to the tensile stresses produced during weld cooling cycle causing decohesion along liquated regions [32]. The absence of microfissuring is mainly due to low heat input on C2 (0.699 kJ/mm) and low tensile stresses produced.

The formation of liquation in HAZ is a common phenomenon in Ni–Cr–Mo alloy. Microfissuring occurs only when the tensile stresses created during cooling causes decohesion along grain boundaries. EDS elemental mapping confirms the presence of Mo-rich precipitates. Generally at low heat input, CMT produces small HAZ zone which results

in minimal intergranular liquation in HAZ. This is the reason behind low amount of tensile stresses produced during welding.

The nature of crack has been revealed. The Fig. 8 shows the micrograph of the HAZ zone closer to the interface. Generally nearer to the interface zone, the austenitic grains far away are larger and nearer to crack are smaller. This is because region close to interface are exhibited to high temperatures due to austenisation followed by growth of grains. Due to increased austenisation, complete dissolution of carbides and formation of harder martensite are observed. This is the reason for the decreased hardness as the prior grains approach crack region and crack cannot propagate through the grains resulting in lower hardness.

From the previous studies, the contraction of the bead during solidification and sudden cooling to preheat temperature results in thermal contraction which is resisted by the substrate end up in tensile residual stress in transverse direction. This causes generation of high tensile stresses at the substrate.

In this work, hence depth/volume of austenite formation and subsequent martensite is small, it produces lower stress generation. The reason claiming to reduction in thickness of martensite layer and thus small cracks appear. Since Ni–Cr–Mo alloy is characterised by low residual stress. The very less amount of residual stress leads to small cracks on the PMZ zone (Fig. 8).

3.3 X‑ray Diffraction

The formation of γ–Ni phase called as the base phase of Ni-based superalloy is confirmed from the XRD results shown in Fig. 10. The γ, γ′, γ″ phases and MC carbide are related to the peaks, hence γ′, γ″ phases and MC carbides are difficult to be identified. Since these phases are present in lower quantities, becomes a reason for not recognising them.

Taking EDS for the dark gray areas (B), it was found to be rich in Mo, Cr, Nickel and Nb shown in Fig. 11.

Figure 12 shows that grains are present in the dark gray area (B), in between the dark gray area are the light gray area (A) and dark particles that envelope the light gray areas. The white particles seen alongside are found to be Nb-rich, contains Nickel, Ti, Mo, Cr. Figure 12 (E) depicts the black blades rich in Cr, Nb, Mo and Ni. XRD analysis of Inconel 625 cladded region have been shown in Fig. 11. From the Electron Dispersive Spectrometry analysis results, area B contains 41.78 wt% nickel, 19.90 wt% Cr, 23.40 wt% Mo and elements such as Nb, Fe, W and Ti. In the non-magnetic phase, the continuous matrix phase γ comprises of FCC structure, containing higher percent of solid solubility alloying elements like iron, Cr, Mo and tungsten. The γ phase is the prime phase of any Ni-based alloy [4, 5, 19, 28]. From the findings of XRD, region B has the phase γ. Since weight

Fig. 9 a SEM micrograph showing Mo-rich precipitate, **b** EDAX showing percentage composition present, **c** EDS pattern showing Mo content in sample C1

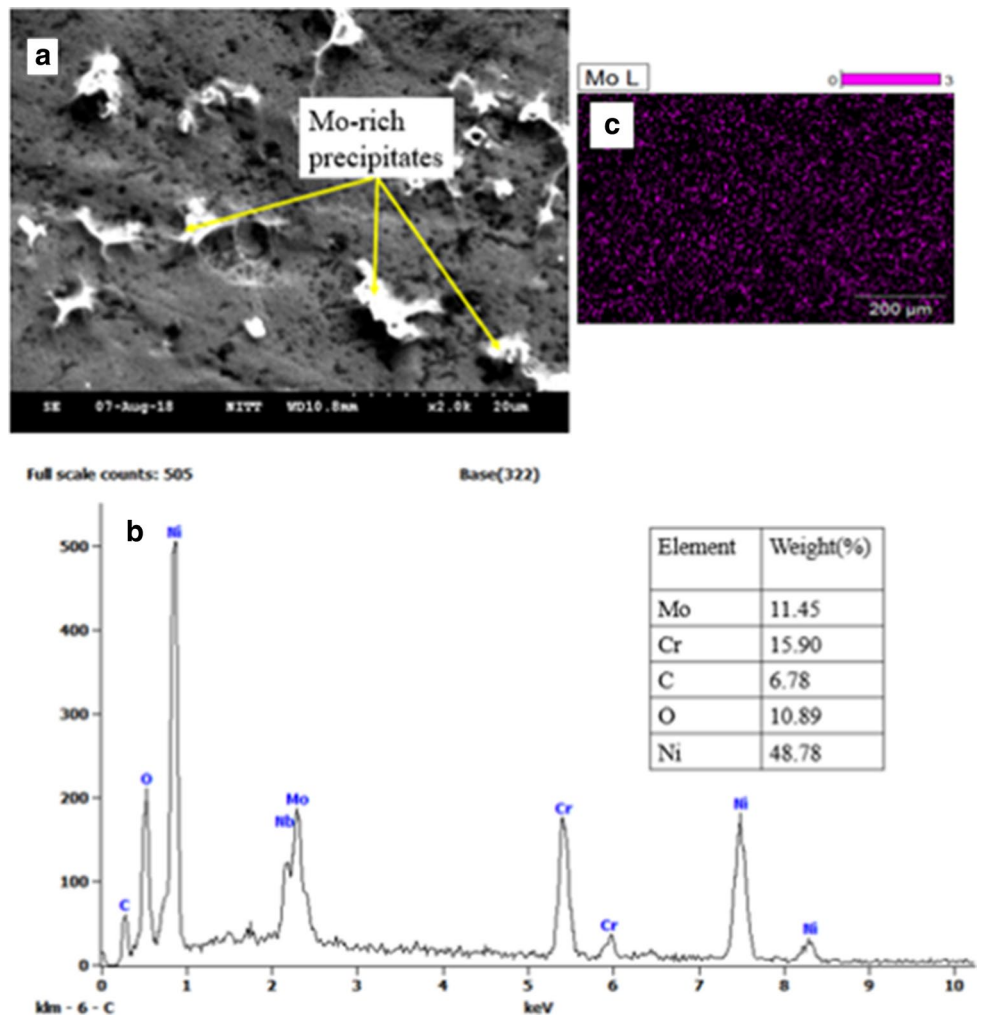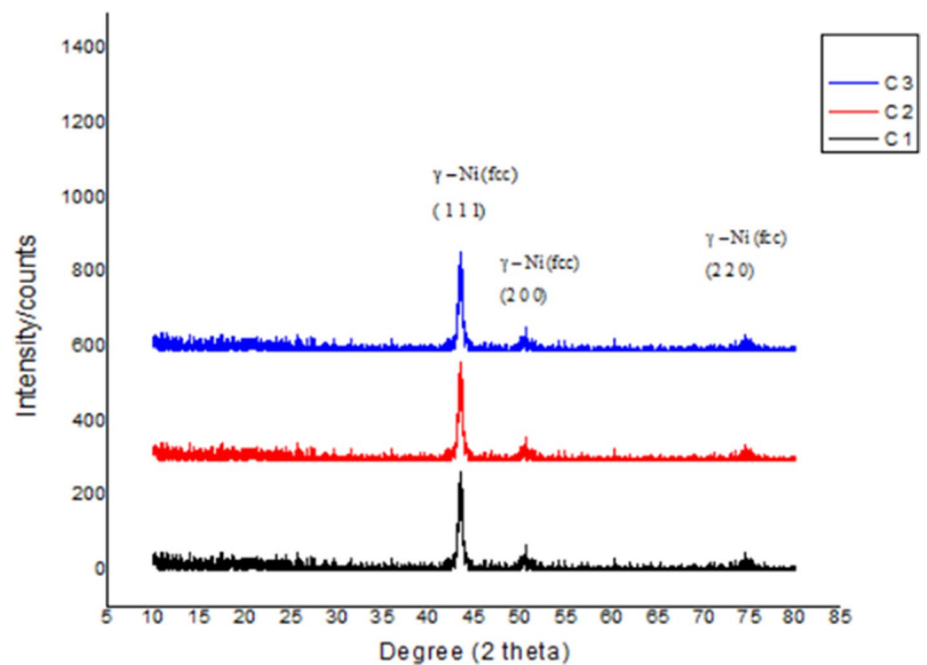| Element	Weight(%)
Mo	11.45
Cr	15.90
C	6.78
O	10.89
Ni	48.78

Fig. 10 XRD spectrum for clad beads C1, C2 and C3 containing Inconel 625 cladded over 316L
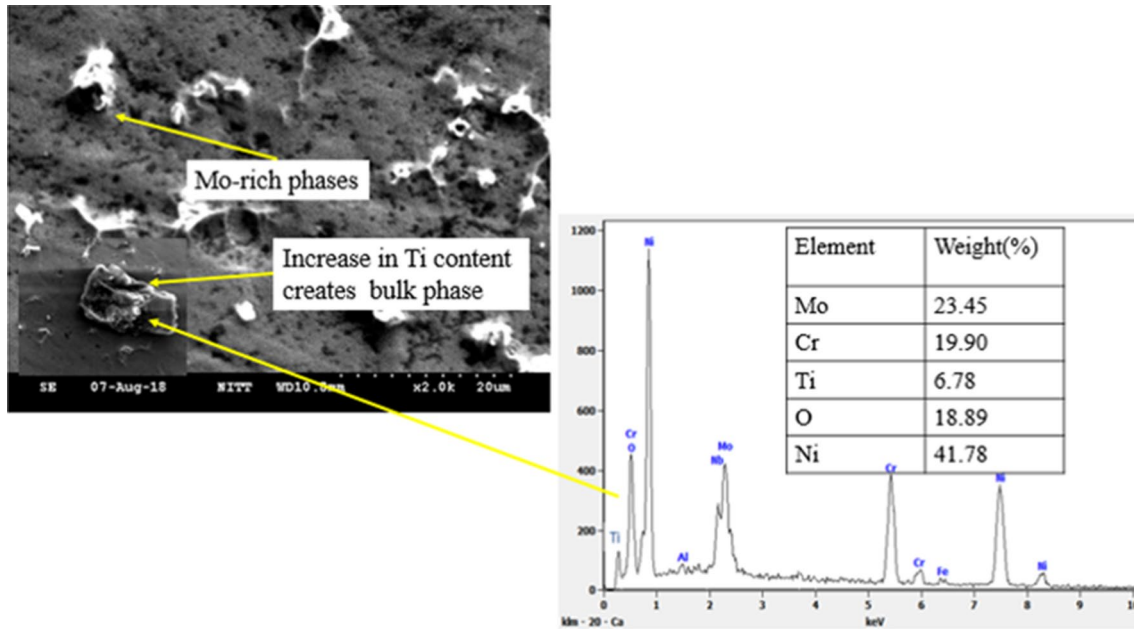
Fig. 11 SEM micrograph showing increase in Ti content forming a bulk phase

percent of elements in region (E) is closer to the region (B), there is a chance for the formation of γ phase.

Formation of carbides is visible in region (C), which is confirmed by the presence of Cr and carbon. Taking region A, 41.7 wt% Ni, 19.90 wt% Cr and 23.45 wt% Mo and 13 wt% niobium were identified. The elements present in the intermetallic compound Ni_3Nb, lies coherent to the γ phase leading to the formation of the phase γ′ or γ″. The low thermal gradient in the coaxial region is the reason for the continuous lave phase. γ dendritic phase appears in the solidification of Inconel 625, where the Nb and Mo elements

move away from the dendrite center and joins the molten region round the dendrite. Also elements like Ni, Cr and Fe transmigrate towards γ dendrites. The increased amount of Mo and Nb in the molten state during solidification gives rise to eutectic compound γ/Laves.

3.4 Microhardness Measurement

Traverse microhardness readings resulted from the Inconel 625 clad region to the lower part of the base metal measured with the help of Vickers micro hardness indentation with a 500 gf applied load and a dwell time of 10 s. The microhardness values of sample C1–C3 in Fig. 13 observes a sharp decrease in the hardness value of the sample across the interface. Vickers microhardness measurements matches with the findings obtained from the metallurgical characterisation and confirmed through SEM images, exhibiting homogenous microstructural features along the interface. 265 ± 25 $HV_{0.5}$, 200 ± 20 $HV_{0.5}$ and 190 ± 15 $HV_{0.5}$, are the resulted hardness value corresponding to clad, interface and base region respectively.

No significant changes in the hardness values is observed. The lower heat input and fast cooling rate tends to decrease the primary dendritic arm spacing, which may be the reason for the increase of hardness value in clad region. The higher hardness value at Inconel 625 clad portion is mainly because of the enrichment of Cr, Nb, Mo and C.

Taking Hall–Petch relationship into account, the hardness value tends to decrease with increase of grain size at room temperature. For a solid solution strengthened superalloy
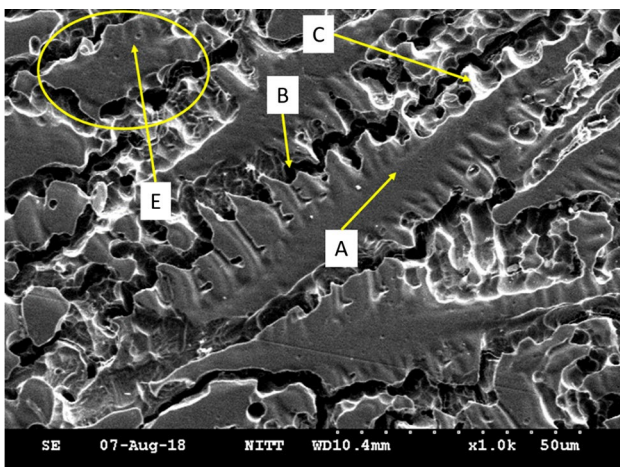

Fig. 12 SEM micrographs revealing the dark and light areas rich in Mo, Cr, Ni and Nb
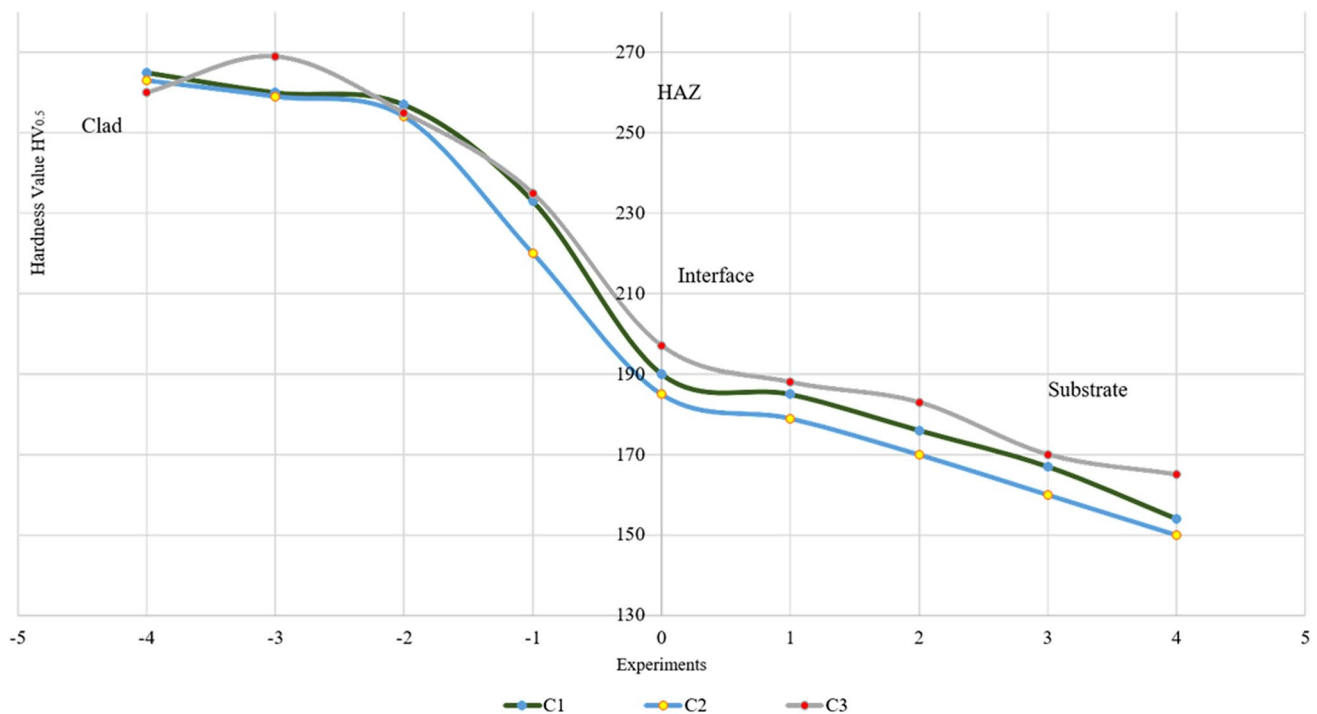
Fig. 13 Microhardness profile of the experiments

like Ni–Cr–Mo alloy, major factor elements which decide the hardness are Mo and Nb. From the confirmation results from SEM/EDS the higher hardness is attributed due to the finer microstructure and impact of segregation of precipitates like Mo and Nb. The dissolution of carbides inside the grains and Mo-rich precipitates along the grain boundaries are the reason behind the variation of hardness in the clad region [36].

The presence of carbides and intermetallics also contribute to higher hardness. In addition to the growth of columnar microstructures nearer to the fusion boundary zone and the hard intermetallics also enhance the hardness along the clad region. The indentation mark impinged on the clad area indicates better bonding between the particles.

The hardness of carbides namely MC is also higher, which can improve the resistance to deformation.

The Laves phase morphology exhibits slightly lower hardness value, but hardness along the clad region increases with increase in speed. Thus it is revealed that, eutectic carbides MC formed as hard particles to hamper the grain boundary dislocation, gives out improved hardness.

3.5 Tensile Testing Results

The summarised results of the tensile tests for cladded samples are observed in Table 5. The samples C1, C2 and C3 respectively are tested and graphs between their stress and strain indicated in Fig. 14. From the stress–strain curves, the ultimate tensile strength, percentage of elongation and yield strength are calculated and drawn in Table 5. From the figure, the highest tensile strength falls on the cladded zone (907 MPa) and the tensile strength of interface zone (721 MPa) which is higher than that of base material (704 MPa). Taking percentage of elongation into consideration, elongation of base material (56.1%) is critically higher than that of cladded zone (29.8%). The yield strength of Inconel 625 cladded zone (533) is slightly increased than the interface zone (433).

From the Table 5, C denotes Clad portion, I denotes Interface portion and B denotes Base portion.

Considering the cladded zone, as the tensile strength attains 907 MPa, showing good bonding and high temperature mechanical characteristics. Higher the tensile strength in the cladded area implies good bonding between the substrate and clad with no defects.

It is concluded that the hardness values and the tensile results match each other in case of dissimilar cladding. Considering past literatures tensile failures peep through in case of AISI 416 attributing to low hardness and strength. Here, with Inconel 625 negligible traces of failure occured in HAZ claiming to the presence of carbon enriched martensite which gave enough strength.

Table 5 Tensile results of the clad, interface and substrate for C1, C2 and C3 samples

Sample type	Sample no.	Yield tensile strength (MPa)	Ultimate tensile strength (MPa)	Elongation (%)
C1	C1 C	533	907	29.8
	C1 I	421	721	33.6
	C1 B	430	704	56.1
C2	C2 C	551	906	35.2
	C2 I	464	795	34.3
	C2 B	439	713	55.1
C3	C3 C	562	971	34.2
	C3 I	482	761	32.5
	C3 B	412	658	58.0

Fig. 14 Curve denoting the stress versus strain plots for samples (C1, C2 and C3) from sliced tensile specimens taken along clad, interface and base region
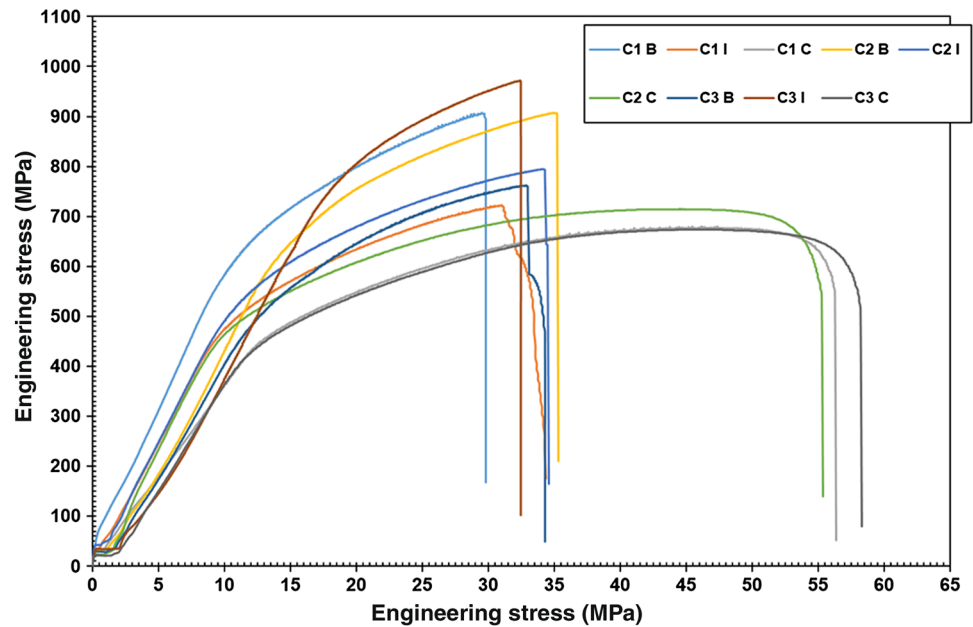
3.6 Fractographic Observation

In general, the nature of fracture depends on the material, temperature, state of stress and rate of loading. Figure 15 shows the fractographic SEM images of samples C1, C2 and C3 respectively. Tear ridges with river markings shown in Fig. 15 occurs due to shear failure which shows a cleavage fracture. The formation of cleavage fracture signifies the chance for the initiation of crack at the grain boundary. The appearance of carbides and intermetallic precipitates present at the grain boundaries serves as the reason for crack initiation.

The ductile mode of fracture in the form of dimpled rupture, exhibited by cup and cone-like depression is shown in Fig. 16a. This reveals that fracture occurs mainly due to density in slip planes in crystal orientation. The secondary precipitates are the major reason for the occurrence of macrovoids [35]. But the secondary intermetallic phases
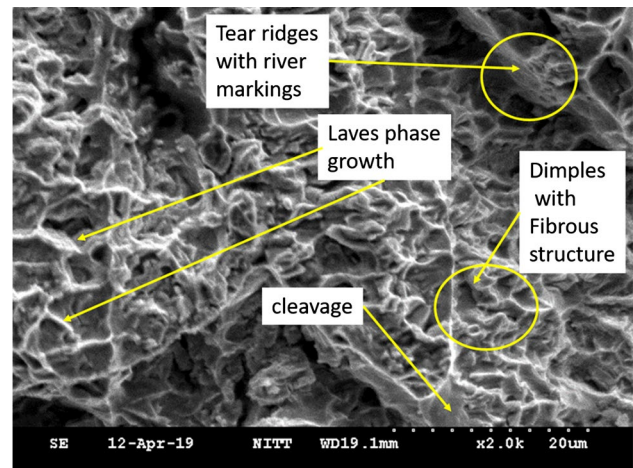
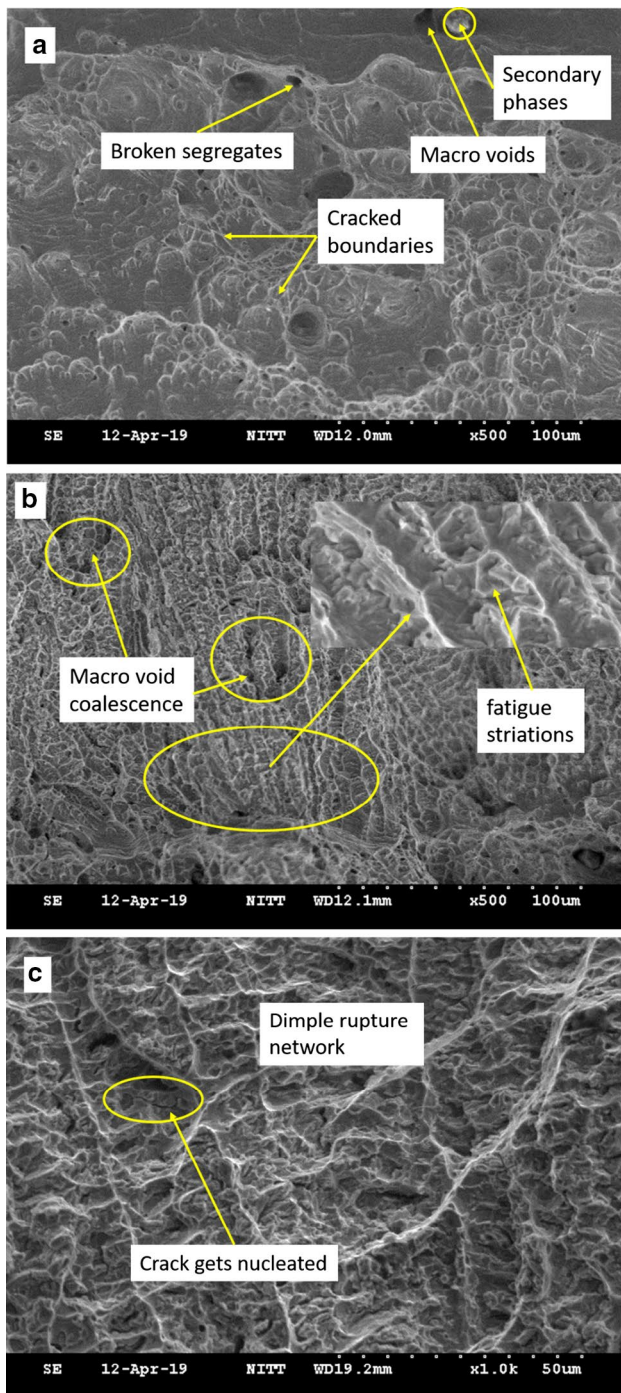**Fig. 15** SEM fractography taken for sample C3 showing cleavage and dimples with fibrous network

Fig. 16 Fractographic images showing macro-void coalescence, fatigue striations and cracked boundaries. (**a**) cup and cone like depression (**b**) macro-void coalescence and fatigue striations (**c**) dimple network

like γ′ and γ″ coalescence, initiate, grow and over a period plastic deformation happens at the intervoids before fracture occurs [15]. From Fig. 16b, it's been clear that fracture initiates from the center of the sample and gets extended by shear separation and the nature of the fracture seems to be fibrous with dimpled network. The appearance of the voids are spherical in nature and of smaller size.

The formation of fatigue striations shown in Fig. 16b reveals that Inconel 625 contains combination of mechanical properties; though it undergoes hardening process and contains a high resistance limit, owing to its nature of ductility, it ends up in bandings. Macrovoid coalescence was seen along the fast fracture region. Figure 16c shows the fracture area of sample prone to a maximum ultimate stress of 742 MPa, which attributed to the formation of subsequent fatigue marks of shear slips and beachmarks. Crack nucleated by the effect of discontinuous surface. The presence of macrovoids coalescence appear mostly in the fast fracture area due to the dimpled network formation.

3.7 Corrosion Potential Tests

The corrosion rate (C_{Rate}), corrosion potential (E_{corr}) and corrosion current density (I_{corr}) are the necessary parameters taken to perform potentiodynamic polarisation tests. The measurement of corrosion potential were done using 3.5% NaCl solution. Table 6 displays the corrosion parameters and their corresponding results in terms of corrosion current density (I_{corr}), corrosion potential (Ecorr) and corrosion rate (C_{Rate}). Table 6 and the corresponding Fig. 17 shows the selected corrosion parameters (for clad and base region). The SEM micrographs showing cross sectioned view of clad and substrate with good bonding in terms of E_{corr}, I_{corr} and C_{Rate}. The corrosion was performed under de aerated 3.5 wt% NaCl solution at 37.4 °C. Compared to the substrate, the clad region exhibits improved resistance to corrosion. The Inconel clad region exhibits passivated region at minimum current density of 4.0×10^{-3} mA cm^{-2} than the substrate which passivated at 1.5×10^{-3} mA cm^{-2}. The formation of passive film layer hampers huge loss of material at maximum current density, thus minimum current density shows an improved corrosion resistance.

The main role of the breakdown potential is to bare the formation of localised attack on the passive film. The wider passive region of clad layer exhibits breakdown potential of 432 ± 5 mV (wrt SCE electrode). The breakdown potential for substrate comes round 270 ± 10 mV (SCE electrode) and a sudden increase in current density with negligible change in potential is observed. This predicts the occurrence of pitting corrosion on the substrate.

Figure 17 shows the potentiodynamic polarization nature of the Inconel 625 cladding, interface area and 316L base area in 3.5% NaCl solution.

Figure 18 shows the results obtained from SEM analysis, pits are noticed on the corroded area and white like flakes indicate the presence of Mo and Nb rich precipitates. The polarisation curve ensures the presence of localised pits on the corroded surface.

Table 6 Corrosion parameters [corrosion potential (E_{corr}), corrosion current density (I_{corr}) and corrosion rate (C_{Rate})] and their results

| Material	Reference electrode	Corrosion performance			
		E_{corr} (mV)	I_{corr} (mA cm^{-2})	R_P (ohm)	C_{Rate} (mm/year)
Base 316L	Saturated calomel electrode (SCE)	-0.4624	0.000157	17,820	0.0005
C1 (worst)	Saturated calomel electrode (SCE)	-0.3396	0.000158	18,900	0.01157
C2	Saturated calomel electrode (SCE)	-0.3914	0.000158	20,004	0.0083
C3 (best)	Saturated calomel electrode (SCE)	-0.2462	0.000452	48,765	0.00330
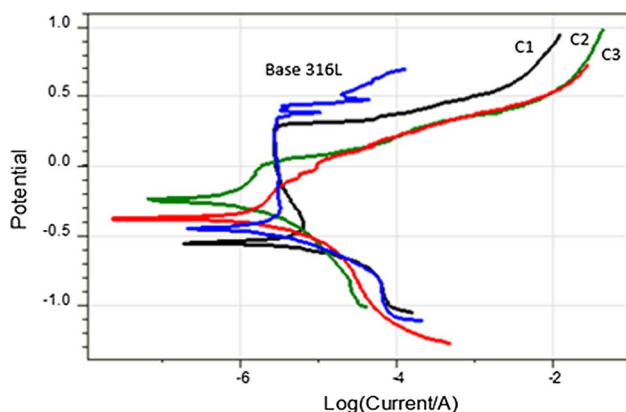
Fig. 17 Potentiodynamic curves Inconel 625 laser clad layers and 316L (as received) substrate in de-aerated 3.5 wt% NaCl solution at 37.4 °C
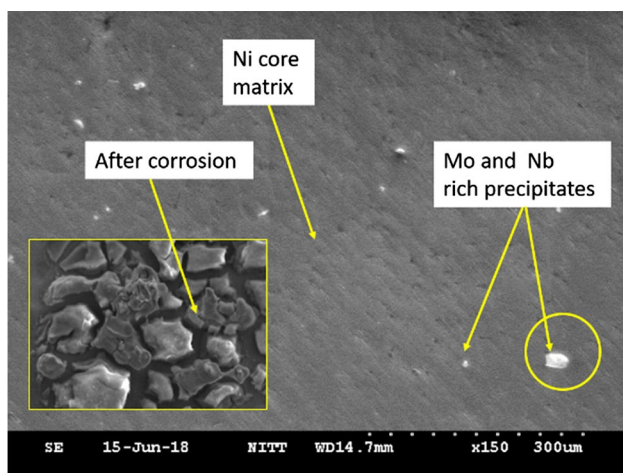

Fig. 18 Mo and Ni rich precipitates scattered as white particles on the Ni matrix

In the transpassive region of the Inconel layer, the current density gradient against potential is very minimum, indicating that passive layer is free from damage nuclei. On comparison of the corrosion potential, clad layer appears to be free from damage [37]. The substrate with Fe content shows minimum breakdown potential, minimum

corrosion potential and maximum passive current density which all indicates minimum corrosion resistance.

The reason is that, the corrosion appears uniformly on the surface of the clad, since no inception of pits on the surface. The matrix area was slightly disturbed due to the dark matrix encompassed by grey corrosion product. But the precipitates remain unaffected [33]. The dendritic matrix acts as sacrificial anode after being attacked by corrosion. Confirmation through SEM on two areas A and B revealed that, the presence of O exhibits that core dendrites suffer oxidation heading to the formation of compounds of Mo shown in Fig. 19. The light grey B contains negligible amount of O, still holding some amount of Nb and Mo. Thus the negligible O and unperceivable change reveals that B is not prone to corrosion attack. The absence of ingress of electrolyte inside the clad layer confirms that substrate is fully protected by Ni–Cr–Mo from the action of corrosion [38].

Considering the Inconel 625 clad zone and interface zone, the base 316L shows slightly higher corrosion potential and their difference among clad, interface and base region is only about 60 mV. Taking Cl-rich environment into consideration, more chances exist for pitting corrosion to occur due to constant pitting potential. At the narrow passive density, the increase of current density with no change in potential is observed. Taking 3.5% NaCl solution, the interface region and substrate show minimum resistance to pitting corrosion than Inconel 625 cladded area. According to Table 6, the increase of corrosion resistance is mainly due to the presence of Cr and Mo-rich Fe–Ni based alloys (Table 7).

As a result, the best corrosion performance in NaCl solution is observed on the Inconel 625 cladded region. Figure 20a, b shows the SEM micrographs of a—sample C3 and b—sample C1 containing Inconel 625 clad region before corrosion tests. In Fig. 20a, b SEM micrographs of sample C3 and C1 before the start of potentiodynmic polarisation test is shown. Samples are polished using SiC papers of grade 600, 800, 1000 and 1200 followed by etching with chemical reagents namely aqua regia (3HNO$_3$: 3HCl).

Similarly in Fig. 21a, b SEM micrographs of sample C3 and C1 after the completion of corrosion tests are shown. The samples C1 and C3 contains dendritic microstructure as shown from both Figs. 20a, b and 21a, b. The grain boundaries are shown by visible bright regions and the columnar dendrite cores are revealed by dark regions seen in Figs. 20a,
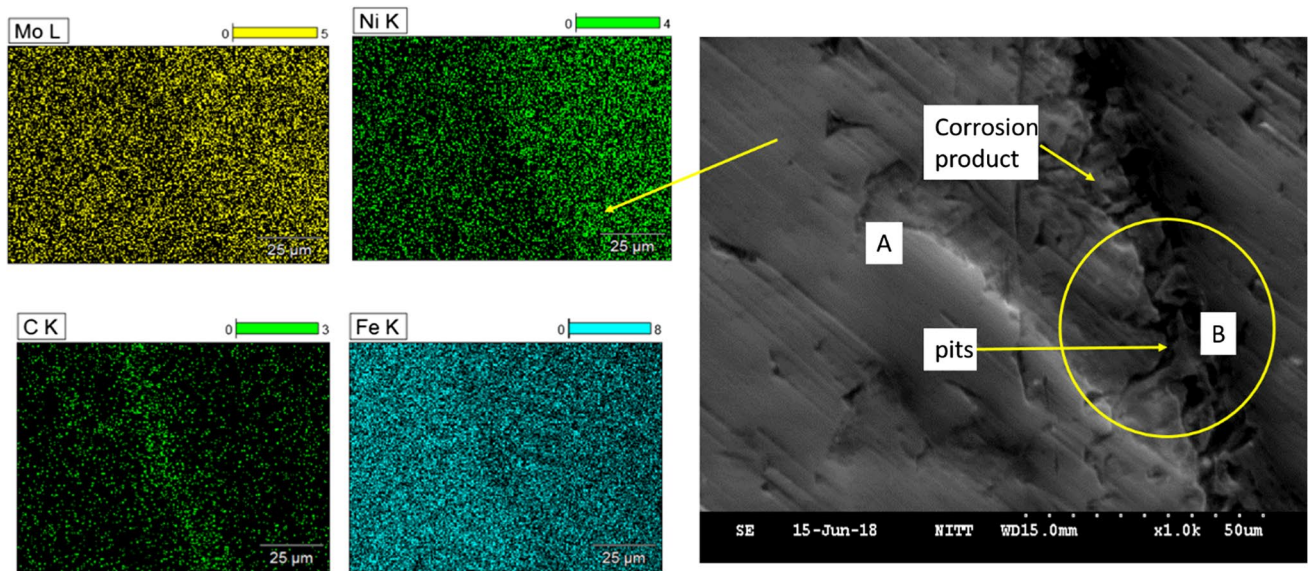
Fig. 19 X-ray mapping done on the clad layer of Inconel 625 after potentiodynamic polarisation test in de-aerated 3.5% NaCl solution

Table 7 Composition analysis (wt%) of two different region A and B identified through SEM in figure

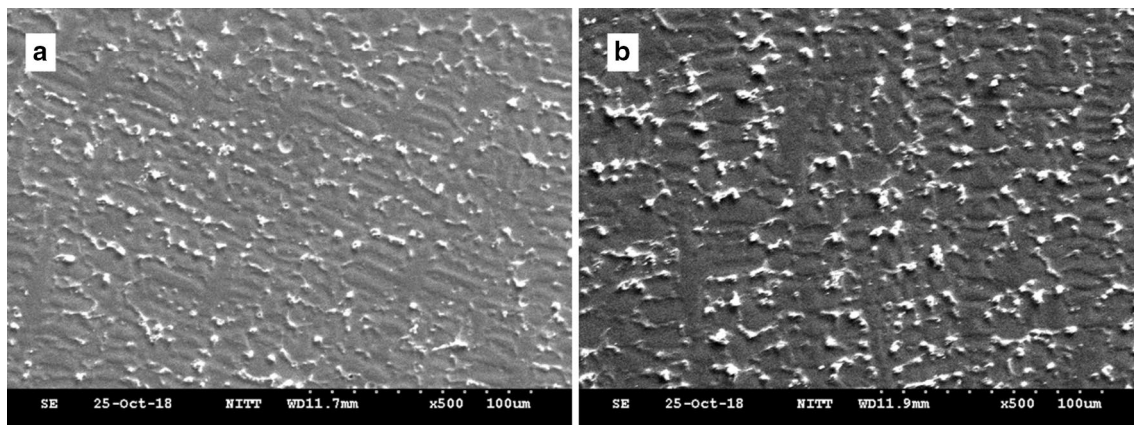| Symbol	O	Cr	Fe	Ni	Nb	Mo
A	16.5	18.7	1.6	42.2	6	14.98
B	3.2	27.6	1.0	58.8	7.3	9.8

Fig. 20 a, b SEM micrograph showing samples **a** sample C3, **b** sample C1 before potentiodynamic polarisation tests

b and 21a, b [26]. The reason for the bright appearance is due to the formation of oxides and Nb carbide on the grain boundaries [28]. Taking sample C1 in Fig. 21b corrosion is visible by the irregular rugged nature of the grain boundary, showing a contrast to sample C1 before corrosion in Fig. 20b.

Figure 22 shows the energy-dispersive X-ray spectroscopy (EDS) examination of chemical composition of elements. Majority of elements as Ni and Cr were found to match with the chemical composition analyzed using the spectrometer. Taking Nb, it was about four times higher at the grain boundary compared to its sourrending, and the Ni, Cr composition comes around 1/3 and 1/2 of those present in the transgranular region.

After corrosion, the shape of the grain boundary can be clearly seen. The presence of corrosion is confirmed by the precipitation of NbC shown in Fig. 23. The corrosion gets initiated along the transgranular region and it is confirmed by
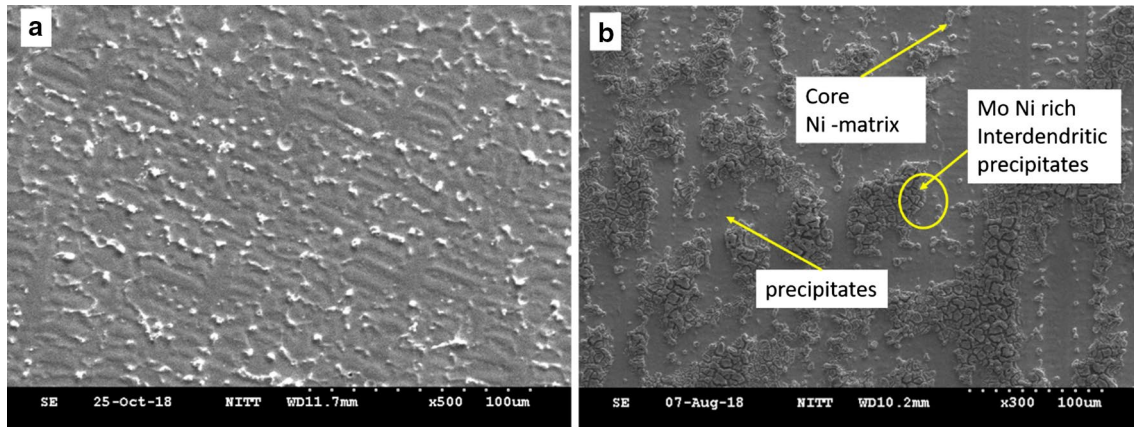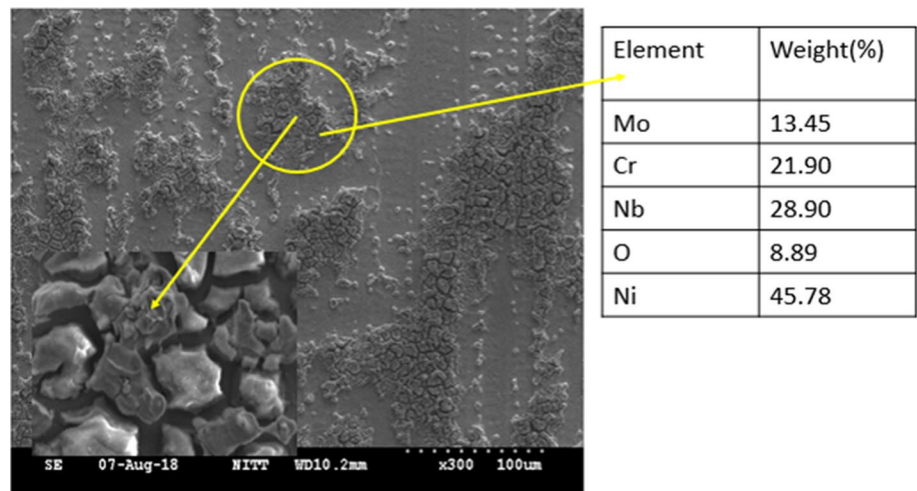
Fig. 21 **a**, **b** SEM micrograph of samples (**a** sample C3, **b** sample C1) soon after the performance of corrosion tests

Fig. 22 EDAX revealing the elemental percentage of Mo, Cr, Nb, Ni present in corroded sample C1

Element	Weight(%)
Mo	13.45
Cr	21.90
Nb	28.90
O	8.89
Ni	45.78

the pit formed on the grain boundary. The sample C3 clearly shows difference from sample C1, the oxides formed appears in bright colour at the subgrain boundaries, indicating the absence of intergranular and overall corrosion. Considering sample C3, not much traces of corrosion is found on the grain boundary [39, 40]. Generally grain boundaries are located from the arrangement on the subgrain boundary, such inferences are not easily identifiable.

Thus the sample C3 found to have 0.00330 mm/yr corrosion rate is obviously less compared to that of sample C1 containing 0.01157 mm/yr corrosion rate. The presence of Cr, Mo and Ni helps in the corrosion resistance in chloride environment and is also the reason for lesser corrosion rate in case of sample C3.
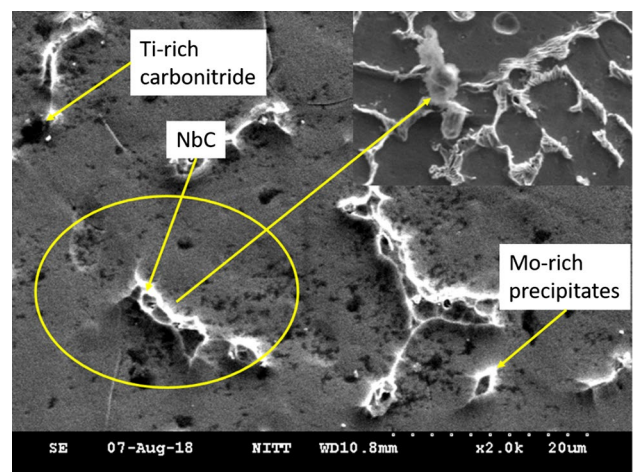

Fig. 23 Presence of Mo-rich precipitates, NbC on sample C3

4 Conclusion

From the results obtained from the metal deposition of Ni–Cr-Mo alloy over 316L austenitic stainless steel using CMT cladding process, the following were drawn:

- Defect and pores free clad beads are obtained from cladding of Inconel 625 over 316L. The welding current of 180 Amps, voltage of 17 volts, torch angle of 80° and travel speed of 175 mm/min, produces minimal dilution (9.3%) and higher clad bead width. The reason for minimal dilution is mainly due to the higher heat input (0.918 kJ/mm) in the Inconel 625 clad region.
- The generic weld morphology comprising of columnar dendritic microstructure along with fine intermetallic precipitates are observed in the clad region. The columnar and coaxial dendrites are observed nearer to clad region towards the interface, coarsened equiaxed grains are seen along the HAZ, columnar and cellular dendrites are observed in the region close to the fusion boundary.
- At low heat input, CMT produces small HAZ zone resulting in minimal intergranular liquation in HAZ. This causes low amount of tensile stresses to be produced.
- Average microhardness indentation value of the clad, interface, base are 265 ± 25 $HV_{0.5}$, 200 ± 20 $HV_{0.5}$ and 190 ± 15 $HV_{0.5}$, respectively. The increase of hardness is attributed mainly due to lower heat input and faster cooling rate, therby causing a reduction the dendritic arm spacing. The presence of carbides and intermetallics also contribute to higher hardness. In addition the growth of columnar microstructures nearer to the fusion boundary and the hard intermetallics also enhance the hardness along the clad region.
- The tensile property of clad area ultimately shows the best results. The tensile strength of interface region shows an elongation 15% higher than substrate is notable. The tensile strength of clad area reaching 706 MPa, indicates its excellent high-temperature property.
- From the fractographic results, the samples mostly comprises of dimpled rupture, exhibited by cup and cone-like depression, nature of fracture appears to be fibrous with dimpled network. The chance for the initiation of crack at the grain boundary is shown from the cleavage type of fracture. The secondary precipitates like γ' and γ'' are the reason behind occurrence of macrovoids.
- From the results of corrosion resistance, the increase is mainly due to higher amount of Mo and Cr in Ni-based alloys. The formation of Cr_2O_3 and the passivation action of the clad zone is due to the presence of Cr.

The solid solution effect in Ni–Cr matrix is contributed by the presence of Nb and Mo. The variation of corrosion resistance depends on the dendritic arm space and finer dendritic arm indicates more corrosion resistance.

References

1. P. Varghese, E. Vetrivendan, M.K. Dash, S. Ningshen, M. Kamaraj, U.K. Mudali, Weld overlay coating of Inconel 617 M on type 316 L stainless steel by cold metal transfer process. Surf. Coat. Technol. **357**, 1004–1013 (2019)
2. O.H. Madsen, New technologies for waste to energy plants, in *4th International Symposium on Waste Treatment Technologies, Babcock & Wilcox Vølund, Sheffield* (2003)
3. T. Baldridge, G. Poling, E. Foroozmehr, R. Kovacevic, T. Metz, V. Kadekar, M.C. Gupta, Laser cladding of Inconel 690 on Inconel 600 superalloy for corrosion protection in nuclear applications. Opt. Lasers Eng. **51**(2), 180–184 (2013)
4. S. Selvi, A. Vishvaksenan, E. Rajasekar, Cold metal transfer (CMT) technology—an overview. Def. Technol. **14**(1), 28–44 (2018)
5. H.T. Zhang, J.C. Feng, P. He, B.B. Zhang, J.M. Chen, L. Wang, The arc characteristics and metal transfer behaviour of cold metal transfer and its use in joining aluminium to zinc-coated steel. Mater. Sci. Eng. A **499**(1–2), 111–113 (2009)
6. P. Kah, M. Shrestha, J. Martikainen, Trends in joining dissimilar metals by welding, in *Applied Mechanics and Materials*, vol. 440, ed. by D. Yang, T. Zhang, Q. Lu (Trans Tech Publications, Zurich, 2014), pp. 269–276
7. A. Schierl, The CMT process a revolution in welding technology. Weld. World Lond. **49**(I), 38 (2005)
8. C.G. Pickin, S.W. Williams, M. Lunt, Characterisation of the cold metal transfer (CMT) process and its application for low dilution cladding. J. Mater. Process. Technol. **211**(3), 496–502 (2011)
9. J. Feng, H. Zhang, P. He, The CMT short-circuiting metal transfer process and its use in thin aluminium sheets welding. Mater. Des. **30**(5), 1850–1852 (2009)
10. M. Solecka, P. Petrzak, A. Radziszewska, The microstructure of weld overlay Ni-base alloy deposited on carbon steel by CMT method, in *Solid State Phenomena*, vol. 231, ed. by B. Dubiel, T. Moskalewicz (Trans Tech Publications, Zurich, 2015), pp. 119–124
11. M. Rozmus-Górnikowska, M. Blicharski, J. Kusiński, Influence of weld overlaying methods on microstructure and chemical composition of Inconel 625 boiler pipe coatings. Met. Mater. **52**(3), 1–7 (2014)
12. J. Tuominen, J. Näkki, H. Pajukoski, T. Nyyssönen, T. Ristonen, T. Peltola, P. Vuoristo, High performance wear and corrosion resistant coatings by novel cladding techniques. Surf. Modif. Technol. **XXVIII**, 13 (2014)
13. A. Evangeline, P. Sathiya, Cold metal arc transfer (CMT) metal deposition of Inconel 625 superalloy on 316L austenitic stainless steel: microstructural evaluation, corrosion and wear resistance properties. Mater. Res. Express **6**(6), 066516 (2019)
14. A. Evangeline, S. Paulraj, Structure–property relationships of Inconel 625 cladding on AISI 316L substrate produced by hot wire (HW) TIG metal deposition technique. Mater. Res. Express (2019). https://doi.org/10.1088/2053-1591/ab350f
15. Q.Y. Wang, Y.F. Zhang, S.L. Bai, Z.D. Liu, Microstructures, mechanical properties and corrosion resistance of Hastelloy C22 coating produced by laser cladding. J. Alloys Compd. **553**, 253–258 (2013)

16. Y. Liang, S. Hu, J. Shen, H. Zhang, P. Wang, Geometrical and microstructural characteristics of the TIG-CMT hybrid welding in 6061 aluminum alloy cladding. J. Mater. Process. Technol. **239**, 18–30 (2017)

17. R.A. Miller, Oxidation-based model for thermal barrier coating life. J. Am. Ceram. Soc. **67**(8), 517–521 (1984)

18. T.E. Abioye, J. Folkes, A.T. Clare, A parametric study of Inconel 625 wire laser deposition. J. Mater. Process. Technol. **213**(12), 2145–2151 (2013)

19. S. Bhattacharya, G.P. Dinda, A.K. Dasgupta, J. Mazumder, Microstructural evolution of AISI 4340 steel during direct metal deposition process. Mater. Sci. Eng. A **528**(6), 2309–2318 (2011)

20. X. Xu, G. Mi, L. Chen, L. Xiong, P. Jiang, X. Shao, C. Wang, Research on microstructures and properties of Inconel 625 coatings obtained by laser cladding with wire. J. Alloys Compd. **715**, 362–373 (2017)

21. S. Saroj, C.K. Sahoo, M. Masanta, Microstructure and mechanical performance of TiC-Inconel825 composite coating deposited on AISI 304 steel by TIG cladding process. J. Mater. Process. Technol. **249**, 490–501 (2017)

22. D. Verdi, M.A. Garrido, C.J. Múnez, P. Poza, Mechanical properties of Inconel 625 laser cladded coatings: depth sensing indentation analysis. Mater. Sci. Eng. A **598**, 15–21 (2014)

23. S.W. Banovic, J.N. DuPont, A.R. Marder, Dilution and microsegregation in dissimilar metal welds between super austenitic stainless steel and nickel base alloys. Sci. Technol. Weld. Join. **7**(6), 374–383 (2002)

24. J.N. DuPont, A.R. Marder, M.R. Notis, C.V. Robino, Solidification of Nb-bearing superalloys: part II. Pseudoternary solidification surfaces. Metall. Mater. Trans. A **29**(11), 2797–2806 (1998)

25. L. Shepeleva, B. Medres, W.D. Kaplan, M. Bamberger, A. Weisheit, Laser cladding of turbine blades. Surf. Coat. Technol. **125**(1–3), 45–48 (2000)

26. G. Longlong, Z. Hualin, L. Shaohu, L. Yueqin, X. Xiaodong, F. Chunyu, Formation quality optimization and corrosion performance of Inconel 625 weld overlay using hot wire pulsed TIG. Rare Met. Mater. Eng. **45**(9), 2219–2226 (2016)

27. T.E. Abioye, P.K. Farayibi, D.G. McCartney, A.T. Clare, Effect of carbide dissolution on the corrosion performance of tungsten carbide reinforced Inconel 625 wire laser coating. J. Mater. Process. Technol. **231**, 89–99 (2016)

28. C.C. Silva, H.C. De Miranda, M.F. Motta, J.P. Farias, C.R.M. Afonso, A.J. Ramirez, New insight on the solidification path of an alloy 625 weld overlay. J. Mater. Res. Technol. **2**(3), 228–237 (2013)

29. R.F. Allen, N.C. Baldini, P.E. Donofrio, E.L. Gutman, E. Keefe, J.G. Kramer et al., *Annual Book of ASTM Standards* (ASTM, West Conshohocken, 1998), p. 188

30. N.V. Rao, G.M. Reddy, S. Nagarjuna, Weld overlay cladding of high strength low alloy steel with austenitic stainless steel–structure and properties. Mater. Des. **32**(4), 2496–2506 (2011)

31. O.T. Ola, F.E. Doern, A study of cold metal transfer clads in nickel-base INCONEL 718 superalloy. Mater. Des. **57**, 51–59 (2014)

32. Y. Kaya, N. Kahraman, An investigation into the explosive welding/cladding of Grade A ship steel/AISI 316L austenitic stainless steel. Mater. Des. **1980–2015**(52), 367–372 (2013)

33. H.N. Moosavy, M.R. Aboutalebi, S.H. Seyedein, An analytical algorithm to predict weldability of precipitation-strengthened nickel-base superalloys. J. Mater. Process. Technol. **212**(11), 2210–2218 (2012)

34. C. Fink, M. Zinke, Welding of nickel-based alloy 617 using modified dip arc processes. Weld. World **57**(3), 323–333 (2013)

35. D. Janicki, Laser cladding of Inconel 625-based composite coatings reinforced by porous chromium carbide particles. Opt. Laser Technol. **94**, 6–14 (2017)

36. L.Y. Xu, M. Li, H.Y. Jing, Y.D. Han, Electrochemical behavior of corrosion resistance of X65/Inconel 625 welded joints. Int. J. Electrochem. Sci. **8**, 2069–2079 (2013)

37. K.Y. Chiu, F.T. Cheng, H.C. Man, Corrosion behavior of AISI 316L stainless steel surface-modified with NiTi. Surf. Coat. Technol. **200**(20–21), 6054–6061 (2006)

38. H.Z. Rajani, S.A. Mousavi, F.M. Sani, Comparison of corrosion behavior between fusion cladded and explosive cladded Inconel 625/plain carbon steel bimetal plates. Mater. Des. **43**, 467–474 (2013)

39. X. Xu, G. Mi, L. Xiong, P. Jiang, X. Shao, C. Wang, Morphologies, microstructures and properties of TiC particle reinforced Inconel 625 coatings obtained by laser cladding with wire. J. Alloys Compd. **740**, 16–27 (2018)

40. J. De Damborenea, A.J. Vázquez, B. Fernández, Laser-clad 316 stainless steel with Ni-Cr powder mixtures. Mater. Des. **15**(1), 41–44 (1994)

Publisher's Note Springer Nature remains neutral with regard to jurisdictional claims in published maps and institutional affiliations.